

Cite this: *J. Mater. Chem. A*, 2026, **14**, 18222

# Interface-engineered integration of nickel–iron phosphide with carbon for efficient and stable oxygen evolution in alkaline media

Tao Zhou,<sup>†a</sup> Zhe Liu,<sup>†a</sup> Kyeounghak Kim <sup>b</sup> and Taekyung Yu <sup>\*a</sup>

The development of robust, efficient, and cost-effective electrocatalysts is essential to address the sluggish kinetics of the oxygen evolution reaction (OER) in alkaline water electrolysis. This study prepared a novel nickel–iron phosphide supported on carbon (NiFe–P@C) composite *via* a two-step method: (i) continuous coprecipitation of NiFe-layered double hydroxide (LDH) nanosheets on carbon supports in a Couette–Taylor flow reactor and (ii) phosphidation at elevated temperature. Taylor vortex flow enables uniform and rapid deposition of NiFe LDH onto the carbon surface, thereby promoting interfacial charge transfer and enhancing reaction kinetics. By tailoring the carbon content and optimizing phosphidation parameters, the resulting NiFe–P@C catalyst exhibited enhanced electrocatalytic performance and long-term operational stability in an alkaline electrolyte. Specifically, it delivered a low overpotential of 233 mV at a current density of 10 mA cm<sup>-2</sup> and a Tafel slope of 44.8 mV dec<sup>-1</sup>. Furthermore, *in situ* Raman spectroscopy combined with density functional theory calculations reveals that phosphorus incorporation effectively modulates the electronic structure and promotes the formation of catalytically active surface species during OER. This flow-assisted synthesis strategy provides a scalable, efficient route to high-performance bimetallic phosphide electrocatalysts for alkaline OER applications.

Received 20th February 2026  
Accepted 27th March 2026

DOI: 10.1039/d6ta01534d

rsc.li/materials-a

## 1. Introduction

To address the increasing global energy demand, various strategies for sustainable energy generation have been explored.<sup>1,2</sup> Among them, green hydrogen has emerged as a promising clean fuel, offering high energy density and producing only water as a byproduct upon combustion.<sup>3,4</sup> Depending on the production route, hydrogen can be classified as gray hydrogen, produced from fossil fuel reforming with substantial carbon dioxide emissions, or green hydrogen, generated *via* water splitting without carbon byproducts. The latter is particularly attractive for environmentally conscious industrial applications. Among green hydrogen generation technologies, water electrolysis stands out for its high energy conversion efficiency and ability to produce ultrapure hydrogen on demand.<sup>5,6</sup> Within this process, the oxygen evolution reaction (OER) plays a pivotal role; however, sluggish reaction kinetics and the requirement for large overpotentials ( $\eta$ ) severely hinder overall energy efficiency.<sup>7,8</sup> Although noble metal-based catalysts, such as ruthenium dioxide and iridium dioxide, currently offer excellent OER performance in commercial applications,<sup>9</sup> their high cost and scarcity

substantially hinder large-scale deployment. Consequently, developing low-cost, earth-abundant electrocatalysts with enhanced OER activity and durability is essential for advancing practical water electrolysis.

Recent advances in electrocatalyst research have highlighted the remarkable potential of transition metal-based compounds as efficient OER catalysts.<sup>10,11</sup> In particular, nickel (Ni)–iron (Fe) layered double hydroxides (NiFe LDHs) have attracted considerable attention owing to their two-dimensional (2D) framework, economic viability, and adjustable chemical composition.<sup>12,13</sup> However, their application is limited by poor electrical conductivity and a tendency toward agglomeration. Thus, transforming NiFe LDHs into transition metal phosphides (NiFe–P) offers an effective strategy as this conversion preserves the 2D layered morphology while adjusting the electronic configuration of the metal centers through anion incorporation.<sup>14,15</sup> NiFe–P exhibits high electrical conductivity, a suitable proton affinity, and optimized metal–hydrogen bonding, properties governed by the negatively charged phosphorus (P) species.<sup>16,17</sup> These characteristics make them attractive for OER catalysis.<sup>18,19</sup> Interestingly, phosphide materials readily undergo surface oxidation under ambient conditions, forming thin oxide layers.<sup>20</sup> The resulting oxides serve as active catalytic interfaces for OER, lowering reaction energy barriers and enabling efficient water splitting.<sup>21</sup> Moreover, the *in situ*-formed oxide shell enhances water adsorption and facilitates hydrogen intermediate transfer to the underlying phosphide

<sup>a</sup>Department of Chemical Engineering, College of Engineering, Integrated Engineering Major, Kyung Hee University, Yongin 17140, Korea. E-mail: tkyu@khu.ac.kr

<sup>b</sup>Department of Chemical Engineering, Hanyang University, Seoul 04763, Korea

<sup>†</sup> These authors contributed equally.



core. The intimate contact and electronic coupling between the phosphide core and oxide shell promote synergistic effects that improve OER kinetics and, consequently, the overall efficiency of electrochemical water splitting. Integrating such active phases into conductive carbon matrices further enhances performance by improving morphology control, increasing exposed active sites, and boosting electrical conductivity.<sup>22,23</sup> Collectively, these structural and surface features make phosphide/oxide-carbon hybrids highly promising electrocatalysts for efficient and scalable water electrolysis.

In addition to structural engineering, recent studies have demonstrated that regulating the electronic structure, interfacial charge transfer, and catalytically active sites plays a crucial role in improving electrocatalytic performance.<sup>24,25</sup> For example, Zheng *et al.* reported that V-doped MoS<sub>2</sub> coupled with a silico-tungstic acid electron mediator can significantly accelerate electron transfer and enhance hydrogen evolution kinetics, highlighting the importance of electron-transfer modulation in catalytic reactions.<sup>26</sup> Furthermore, the durability of electrocatalysts under practical operating conditions remains a key challenge, particularly at large current densities relevant to industrial electrolysis. Ge *et al.* developed a Mo-FeCoP@MnO<sub>x</sub>/NF catalyst with a double protection mechanism that effectively improves corrosion resistance and enables stable seawater electrolysis at ampere-level current densities.<sup>27</sup> Meanwhile, growing attention has been devoted to the rational modulation of electronic structure and local coordination environment, which are critical factors for enhancing the catalytic performance of oxygen evolution reaction (OER) catalysts. Recent studies have shown that metal-organic framework-derived nanosheets with optimized charge-transfer characteristics can significantly improve catalytic activity, especially at high current densities.<sup>28</sup> In addition, engineering the coordination environment of transition-metal active sites has been proven to effectively regulate the adsorption energies of key OER intermediates, thereby accelerating reaction kinetics and enhancing catalytic stability.<sup>29</sup> In particular, tailoring the local coordination structure in NiFe-based catalysts can optimize the catalytic pathway and reduce the overpotential required for efficient oxygen evolution.<sup>30</sup> Collectively, these advances demonstrate that precise regulation of the electronic structure, active-site configuration, and structural stability is an effective strategy for achieving high catalytic activity and durability.

Despite the promising electrocatalytic performance of NiFe-based materials, achieving precise nanoscale structural control and uniform dispersion remains challenging, particularly with conventional batch or stirred-tank synthesis methods. To address this limitation, Taylor vortex flow (TVF)—a highly ordered and controllable hydrodynamic regime generated in a Couette-Taylor (CT) reactor—has been proposed.<sup>31,32</sup> When the inner cylinder rotates beyond a critical speed, stable toroidal vortices form, enabling efficient radial mixing, uniform shear fields, enhanced mass transport, and directed molecular motion. These features favor the controlled nucleation and growth of nanomaterials while accelerating reaction kinetics, enabling reproducible and scalable synthesis. Previous studies have demonstrated the successful use of TVF in synthesizing

stabilizer-free metal nanoparticles and luminescent quantum dots at industrially relevant throughputs.<sup>33,34</sup> Building on this concept, this study aims to exploit TVF for the controlled synthesis of NiFe LDH nanosheets supported on conductive carbon (NiFe LDH@C). By fine-tuning parameters such as rotational speed, mean residence time, and precursor concentration, we achieve morphology-controlled and homogeneously distributed NiFe nanostructures—features difficult to achieve conventionally. The versatility of TVF has also been validated in other layered systems, including the exfoliation of graphene and molybdenum disulfide,<sup>35,36</sup> highlighting its broader potential in nanomaterials engineering.

This study fabricated a nickel-iron phosphide supported on carbon (NiFe-P@C) hybrid electrocatalyst through a two-step interfacial design strategy: (i) continuous coprecipitation of NiFe LDH onto carbon substrates using a CT reactor and (ii) *in situ* phosphidation to transform the hydroxides into bimetallic phosphides. This architecture improves electrical conductivity, increases the density of catalytically active sites, and suppresses the aggregation and delamination of active phases during prolonged electrochemical operation. A comprehensive study was performed to elucidate the effects of the Ni/Fe molar ratio, carbon loading, and crystallinity on structural features, morphology, and OER performance. The optimized NiFe-P@C catalyst exhibited remarkable OER activity, achieving a low  $\eta$  of 233 mV and a Tafel slope of 44.8 mV dec<sup>-1</sup> at a current density of 10 mA cm<sup>-2</sup> in 1.0 M potassium hydroxide (KOH). Furthermore, *in situ* Raman spectroscopy revealed the rapid formation of surface-active  $\gamma$ -NiOOH species during OER, which are closely linked to improved catalytic activity. Density functional theory (DFT) calculations further showed that P incorporation modulates the electronic structure of NiFe LDH, improving electrical conductivity and optimizing surface electronic properties, thereby contributing to superior OER performance. Compared with the pristine NiFe LDH precursor, the phosphide composite demonstrated markedly enhanced performance, highlighting its potential as a low-cost and efficient electrocatalyst for scalable water splitting and renewable energy applications.

## 2. Experimental

### 2.1. Materials

Nickel nitrate hexahydrate (Ni[NO<sub>3</sub>]<sub>2</sub>·6H<sub>2</sub>O), iron nitrate nonahydrate (Fe[NO<sub>3</sub>]<sub>3</sub>·9H<sub>2</sub>O), sodium hydroxide (NaOH), formamide, a 5% Nafion™ 117 solution, and sodium hypophosphite monohydrate (NaH<sub>2</sub>PO<sub>2</sub>·H<sub>2</sub>O) were all obtained from Sigma-Aldrich and used directly without further purification. Vulcan XC-72 carbon black was procured from Macklin.

### 2.2. Synthesis of NiFe LDH@C via a continuous CT reactor

NiFe LDH@C composites were synthesized using a CT reactor (Fig. 1). This setup comprises a stationary outer cylinder and a rotating inner cylinder, with an effective working volume of 12.2 mL. Detailed structural parameters of the reactor components are provided in Table S1 (SI). Ni(NO<sub>3</sub>)<sub>2</sub>·6H<sub>2</sub>O and



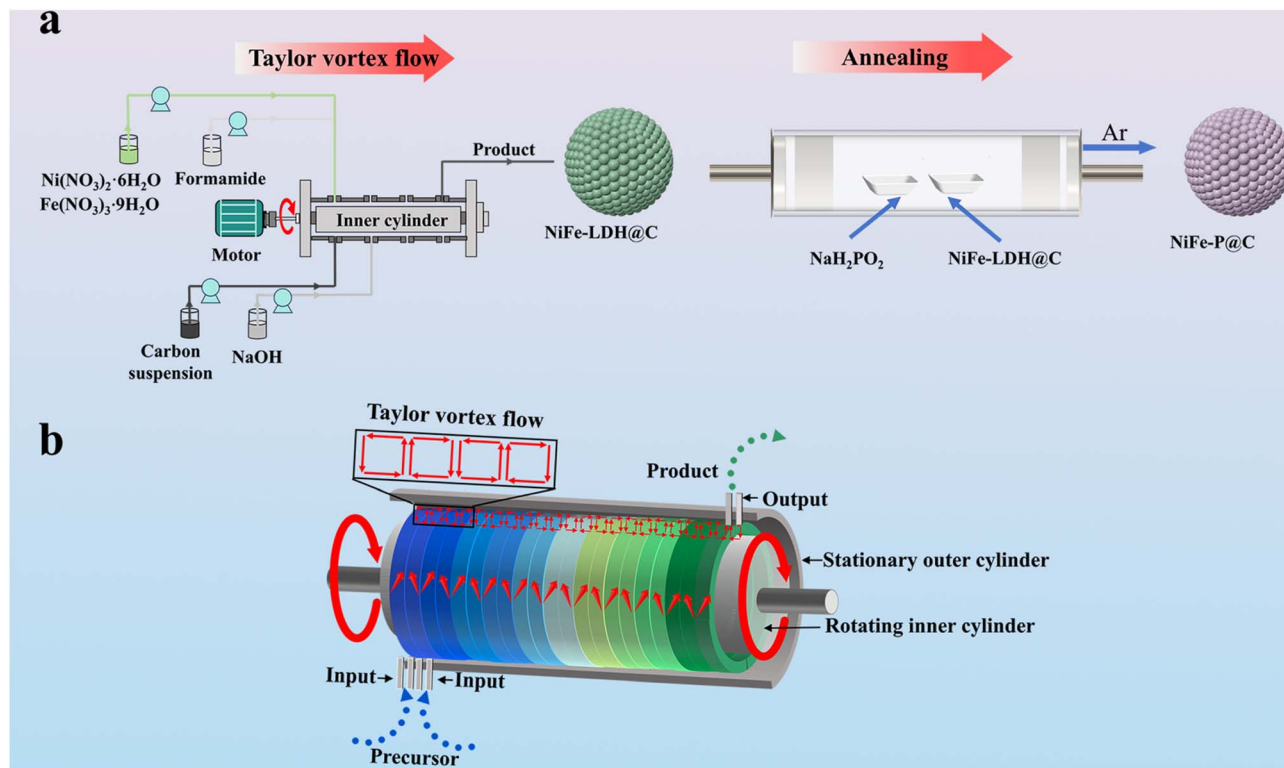


Fig. 1 Schematic of NiFe-P@C electrocatalyst preparation. (a) Experimental setup for synthesizing NiFe LDH on carbon (NiFe LDH@C) via the CT reactor and the annealing condition. (b) Shear-assisted synthesis mechanism driven by CT flow.

Fe(NO<sub>3</sub>)<sub>3</sub>·9H<sub>2</sub>O served as Ni and Fe precursors, respectively, while Vulcan XC-72 carbon black was used as the support. Formamide was added to reduce excessive layer stacking of LDHs during coprecipitation. After prefilling the reactor with deionized water and achieving steady rotation, four feed solutions were continuously introduced *via* three independent channels using peristaltic pumps: a carbon dispersion (10.0 mg mL<sup>-1</sup>), NaOH (1.25 mM), formamide (23 vol%), and a metal ion solution containing 0.2 M Ni<sup>2+</sup> and 0.066 M Fe<sup>3+</sup>. The carbon suspension flow rate was 13.5 mL min<sup>-1</sup>, while the other three feeds were supplied at 1.2–1.8 mL min<sup>-1</sup>. TVF at 1200 rpm ensured uniform mixing and controlled nucleation. After maintaining flow conditions for 10 residence times (approximately 2 min per cycle), the resulting dispersion was collected, centrifuged at 8000 rpm, and washed thoroughly with deionized water. The solids were vacuum-dried at 50 °C for 6 h. To evaluate the effect of carbon content, the flow rate of the carbon suspension was varied: 9.0 mL min<sup>-1</sup> for NiFe LDH@C-200, 4.5 mL min<sup>-1</sup> for NiFe LDH@C-100, and 2.25 mL min<sup>-1</sup> for NiFe LDH@C-50. Here, NiFe LDH@C-50 denotes 100 mg of NiFe LDH loaded onto 50 mg of carbon, whereas NiFe LDH@C-100 corresponds to 100 mg of NiFe LDH supported on 100 mg of carbon. Unless otherwise specified, all carbon-containing samples were prepared with a fixed carbon loading of 300 mg; for example, NiFe LDH@C refers to 100 mg of NiFe LDH on 300 mg of carbon (denoted as NiFe LDH@C-300), and NiFe-P@C indicates a material synthesized using 300 mg of carbon support. For comparison, Ni(OH)<sub>2</sub>@C and Fe(OH)<sub>3</sub>@C were

synthesized using the same procedure, excluding the Fe and Ni precursors, respectively. A control sample of NiFe LDH was also obtained without carbon support.

### 2.3. Synthesis of NiFe-P@C

Metal phosphides were synthesized *via* a phosphidation process. Specifically, NiFe LDH@C and NaH<sub>2</sub>PO<sub>2</sub>·H<sub>2</sub>O were placed separately in two ceramic boats within a tubular furnace, with NaH<sub>2</sub>PO<sub>2</sub>·H<sub>2</sub>O positioned upstream and NiFe LDH@C downstream. The system was purged with argon to maintain an inert atmosphere. The furnace was heated to 350 °C at 2 °C min<sup>-1</sup>. After holding at this temperature for 2 h, the furnace was cooled naturally to room temperature. The resulting product, designated NiFe-P@C, was collected for further characterization.

### 2.4. Synthesis of Ni-P@C, Fe-P@C, and NiFe@C

Ni-P@C and Fe-P@C were prepared following the same phosphidation procedure as NiFe-P@C, using Ni(OH)<sub>2</sub>@C and Fe(OH)<sub>3</sub>@C precursors, respectively. For NiFe@C, the NiFe LDH@C precursor underwent identical annealing conditions under an argon atmosphere without NaH<sub>2</sub>PO<sub>2</sub>·H<sub>2</sub>O, thereby excluding phosphidation.

### 2.5. Characterization

Morphology and nanostructure size were examined using transmission electron microscopy (TEM; JEM-2100 F, Japan).



The elemental composition was quantified using inductively coupled plasma mass spectrometry (Leeman, USA). Crystallographic information was obtained *via* X-ray diffraction (XRD; Rigaku D-MAX/A, Japan) operated at 35 kV and 35 mA with copper  $K\alpha$  radiation ( $\lambda = 1.5418 \text{ \AA}$ ). Surface chemical states and electronic environments were investigated by X-ray photoelectron spectroscopy (XPS; PHI 5000 VersaProbe, Japan) using a monochromatic aluminum  $K\alpha$  source.

## 2.6. Electrochemical measurements

Electrochemical measurements were conducted on a CHI 760E workstation in 1.0 M KOH electrolyte using a conventional three-electrode setup: a graphite rod counter electrode, Hg/HgO reference electrode, and glassy carbon (GC) working electrode substrate (3 mm diameter). All potentials were converted to the reversible hydrogen electrode (RHE) scale using the following equation:

$$E_{\text{RHE}} (\text{V}) = E_{(\text{vs. Hg/HgO})} + 0.0591 \times \text{pH} + 0.098.$$

For working electrode preparation, 5 mg of the as-synthesized NiFe-P@C powder was dispersed in a mixture of 980  $\mu\text{L}$  ethanol and 20  $\mu\text{L}$  Nafion solution *via* ultrasonication for 20 min to form a homogeneous ink. Subsequently, 12  $\mu\text{L}$  of the ink was drop-cast onto the GC electrode to form the catalytic layer. To ensure a fair comparison with as-synthesized catalysts, including commercial catalysts (RuO<sub>2</sub> and Pt/C), all working electrodes were prepared using an identical procedure. Linear sweep voltammetry (LSV) was performed at a scan rate of 10 mV s<sup>-1</sup> with 90% iR compensation. Cyclic voltammetry (CV) was performed in the potential range of 0.2–0.5 V *versus* a saturated calomel electrode at 50 mV s<sup>-1</sup>. The electrochemically active surface area (ECSA) was estimated from the double-layer capacitance ( $C_{\text{dl}}$ ), determined from CV curves at various scan rates, based on the following equation:

$$\text{ECSA} = C_{\text{dl}}/C_{\text{s}},$$

where  $C_{\text{s}}$  represents the specific capacitance, taken as 0.040 mF cm<sup>-2</sup> in 1.0 M KOH. Electrochemical impedance spectroscopy (EIS) was conducted over a frequency range of 0.1 Hz–1000 kHz at different  $\eta$  to determine solution resistance ( $R_{\text{s}}$ ) and charge transfer resistance ( $R_{\text{ct}}$ ) using an equivalent circuit model. The long-term stability of the catalysts was evaluated by chronopotentiometry ( $V-t$ ) at constant potential.

All electrochemical measurements were carried out under the same experimental conditions. For overall water splitting, a two-electrode configuration was employed, in which NiFe-P@C and Pt/C were used as the anode and cathode, respectively. As a benchmark system, RuO<sub>2</sub> and Pt/C were assembled under the same preparation procedure and catalyst loading to ensure a reliable comparison.

For high-current-density stability tests at 500 mA cm<sup>-2</sup>, the catalyst ink with the same concentration was drop-cast onto a 0.25 cm<sup>2</sup> nickel foam (NF) substrate instead of GCE. This modification was adopted to enhance mechanical stability and

prevent catalyst detachment caused by vigorous bubble generation at large current densities.

The oxygen evolution during the electrocatalytic water oxidation process was monitored using a gas collection system under controlled electrolysis conditions. The electrochemical measurements were performed in a standard three-electrode configuration using 1.0 M KOH electrolyte. During electrolysis, the evolved gas from the anode was collected using a gas-tight setup connected to an inverted graduated cylinder filled with electrolyte solution. For the quantitative measurement, the volume of the evolved gas was recorded as a function of time under a constant applied current. The oxygen production rate was calculated from the slope of the gas volume *versus* time curve. The measured gas volume was corrected for ambient temperature and pressure conditions to obtain accurate oxygen evolution rates. For the qualitative analysis, the collected gas was analyzed using gas chromatography equipped with a thermal conductivity detector to confirm the chemical identity of the evolved gas. The gas chromatography analysis confirmed that the generated gas was oxygen with negligible impurities, indicating that the observed gas evolution originated from the oxygen evolution reaction.

## 2.7. Calculation method

All DFT calculations were performed using the CASTEP module implemented in the Materials Studio package. Electron exchange–correlation effects were treated within the generalized gradient approximation using the Perdew–Burke–Ernzerhof functional.<sup>37</sup> On-the-fly generated ultrasoft pseudopotentials were employed to balance computational efficiency and accuracy. Full geometric optimizations were performed for NiFe-P@C and NiFe LDH@C models. A plane-wave basis set with a kinetic energy cutoff of 400 eV was used, and self-consistent field calculations were converged to  $1.0 \times 10^{-6}$  eV. Geometry optimization was considered converged when the maximum residual force on each atom was below 0.03 eV  $\text{\AA}^{-1}$ . Brillouin zone integrations employed a  $5 \times 5 \times 2$  Monkhorst–Pack  $k$ -point mesh.<sup>38</sup> In addition, maximum atomic displacement and residual stress were constrained below 0.001  $\text{\AA}$  and 0.05 GPa, respectively, to ensure reliable structural relaxation.

# 3. Results and discussion

## 3.1. Preparation and characterization of catalysts

In previous work, we demonstrated that uniform and periodic TVF in a CT reactor enables the synthesis of highly uniform, well-dispersed nanoparticles without stabilizing agents.<sup>33</sup> Toroidal vortices substantially enhance micromixing, thereby increasing nucleation rates and enabling the formation of nanoparticles with small, consistent sizes. Additionally, the persistent shear forces present in the CT reactor effectively inhibit particle aggregation. This study employed a continuous CT reactor to synthesize NiFe LDH supported on Vulcan XC-72 carbon (denoted as NiFe LDH@C). The carbon substrate provides preferential nucleation sites, promoting adsorption



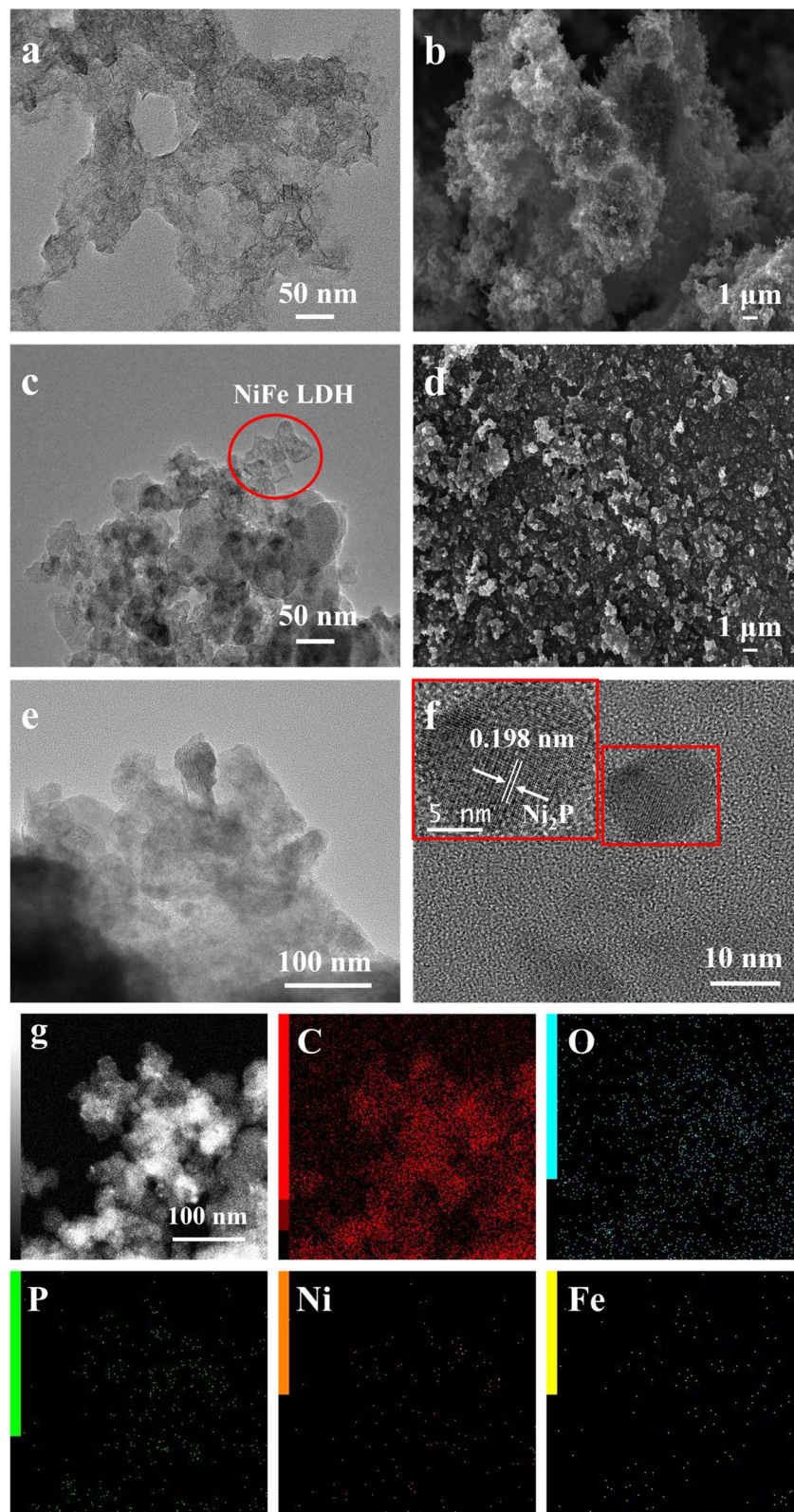


Fig. 2 (a) TEM image of NiFe LDH. (b) SEM and (c) TEM images of NiFe LDH@C. (d) SEM, (e) TEM, and (f) HRTEM images of NiFe-P@C. (g) Elemental mapping images of C, O, P, Ni, and Fe in the NiFe-P@C.

and accumulation of  $\text{Ni}^{2+}$  and  $\text{Fe}^{3+}$  and the formation of surface-bound  $\text{Ni}(\text{OH})_2$  and  $\text{Fe}(\text{OH})_3$  species. During coprecipitation, the reaction mixture pH was maintained at approximately 10 *via*

gradual NaOH addition, thereby establishing the alkaline conditions necessary for the simultaneous precipitation of  $\text{Ni}^{2+}$  and  $\text{Fe}^{3+}$  ions. At this pH, the concentrations of both metal



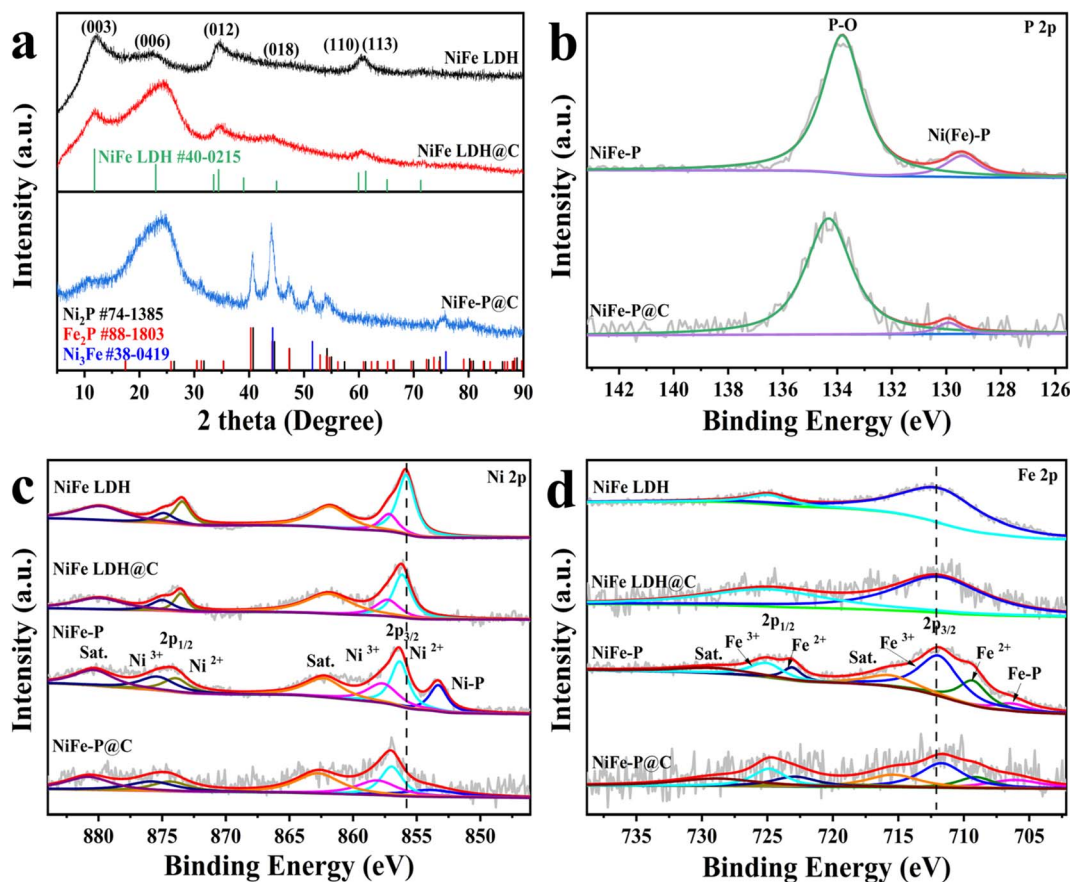


Fig. 3 (a) XRD patterns of NiFe LDH, NiFe LDH@C, and NiFe-P@C. XPS spectra of (b) P 2p, (c) Ni 2p, and (d) Fe 2p for NiFe LDH, NiFe LDH@C, NiFe-P, and NiFe-P@C.

hydroxides surpass their respective solubility product constants, ensuring complete precipitation and preventing premature hydrolysis. Through continuous aggregation and oxidation,  $\text{Ni}(\text{OH})_2$  and  $\text{Fe}(\text{OH})_3$  monomers progressively crystallize into NiFe LDH nanosheets on the carbon substrate. Heterogeneous nucleation sites may lead to irregular orientation and arrangement of the nanosheets. Finally, the as-prepared NiFe LDH@C was phosphidated in a tubular furnace to yield NiFe-P@C.

As shown in Fig. 2a, pristine NiFe LDH nanosheets aggregate owing to their high surface energy, limiting the utilization of the available surface area and active sites. In contrast, NiFe LDH@C displays a more homogeneous, interconnected architecture that enhances electrolyte diffusion and promotes efficient charge and mass transport during OER (Fig. 2b and c).<sup>39</sup> Elemental mapping results confirm uniform distribution of Ni, Fe, O, and C within NiFe LDH@C (Fig. S1). Notably, oxygen originates from hydroxide groups and oxides formed during coprecipitation. The uniform dispersion of LDH nanosheets on the carbon matrix effectively mitigates aggregation and indicates a strong interfacial interaction between the active phase and conductive support. Following phosphidation, NiFe-P@C largely retains its network structure, demonstrating high structural stability during thermal conversion (Fig. 2d and e). High-resolution TEM (HRTEM) images show well-resolved lattice fringes (Fig. 2f),

with an interplanar spacing of 0.198 nm corresponding to the (201) planes of  $\text{Ni}_2\text{P}$ .<sup>40</sup> A uniform distribution of Ni, Fe, P, C, and O across the nanosheets was verified by EDS mapping (Fig. 2g). The observed morphological contrast between NiFe-P@C and bulk NiFe-P emphasizes the critical contribution of the carbon substrate in enhancing dispersion and retaining high surface area. Additionally, uniform P incorporation confirms successful phosphidation. Notably, some residual oxides are inevitably formed during the high-temperature transformation from LDH to phosphide.

The XRD pattern of pristine NiFe LDH exhibits several weak reflection peaks at  $12.2^\circ$ ,  $22.5^\circ$ ,  $34.6^\circ$ ,  $44.3^\circ$ , and  $60.7^\circ$ , corresponding to the (003), (006), (012), (018), and (110) lattice planes of the LDH structure, respectively (JCPDS No. 40-0215, Fig. 3a).<sup>41</sup> These peaks confirm the successful synthesis of NiFe LDH *via* the continuous CT reactor, and their relative sharpness indicates well-developed crystallinity. In NiFe LDH@C, a distinct peak at  $24.2^\circ$  appears, attributable to the (002) plane of carbon, confirming deposition of LDH nanosheets onto the carbon substrate. This effect is attributed to steric hindrance introduced by the nanosheets on the surface. Moreover, the enhanced (018) reflection suggests that the carbon support promotes NiFe LDH crystallization, potentially *via* epitaxial alignment with the underlying carbon framework.<sup>42</sup> Upon phosphidation, the diffraction peaks associated with the LDH



structure disappear, implying full phase transformation. To further resolve the complex phase constitution of the resulting phosphides, slow-scan XRD ( $2^\circ \text{ min}^{-1}$ ) was performed for NiFe-P@C. Two dominant reflections at  $51.5^\circ$  and  $75.8^\circ$  correspond to the (200) and (220) planes of  $\text{Ni}_3\text{Fe}$  (JCPDS No. 38-0419),<sup>43</sup> while the peak at  $24.2^\circ$  arises from graphitic carbon. Additional peaks at  $40.6^\circ$ ,  $43.9^\circ$ ,  $47.2^\circ$ , and  $54.5^\circ$  are indexed to the (111), (201), (210), and (300) planes, respectively. These reflection peaks fall between those of  $\text{Ni}_2\text{P}$  (JCPDS No. 74-1385)<sup>44</sup> and  $\text{Fe}_2\text{P}$  (JCPDS No. 88-1803),<sup>45</sup> confirming the formation of a bimetallic NiFe phase. Overall, these results indicate the successful synthesis of carbon-supported NiFe phosphide composites.

Further insights into the chemical environment and oxidation states of elements in NiFe-P@C were obtained *via* XPS. The wide-scan spectra confirm the coexistence of Ni, Fe, P, O, and C, consistent with previous EDS results (Fig. S2). The high-resolution P 2p spectra display a peak at 129.8 eV corresponding to metal (Fe and Ni) phosphides (Fig. 3b), while a second notable peak at 134.3 eV is attributed to oxidized P (P-O), likely from the surface oxidation of phosphides exposed to air.<sup>46,47</sup> The Ni 2p region shows peaks at 857.0 and 874.4 eV assigned to  $\text{Ni}^{2+}$   $2p_{3/2}$  and  $2p_{1/2}$  states (Fig. 3c).<sup>48</sup> Additionally, peaks at 858.1 and 875.8 eV are attributed to  $\text{Ni}^{3+}$  species.<sup>49</sup> A distinct signal at 853.9 eV indicates Ni-P bonding in  $\text{Ni}_2\text{P}$ , with satellite peaks at

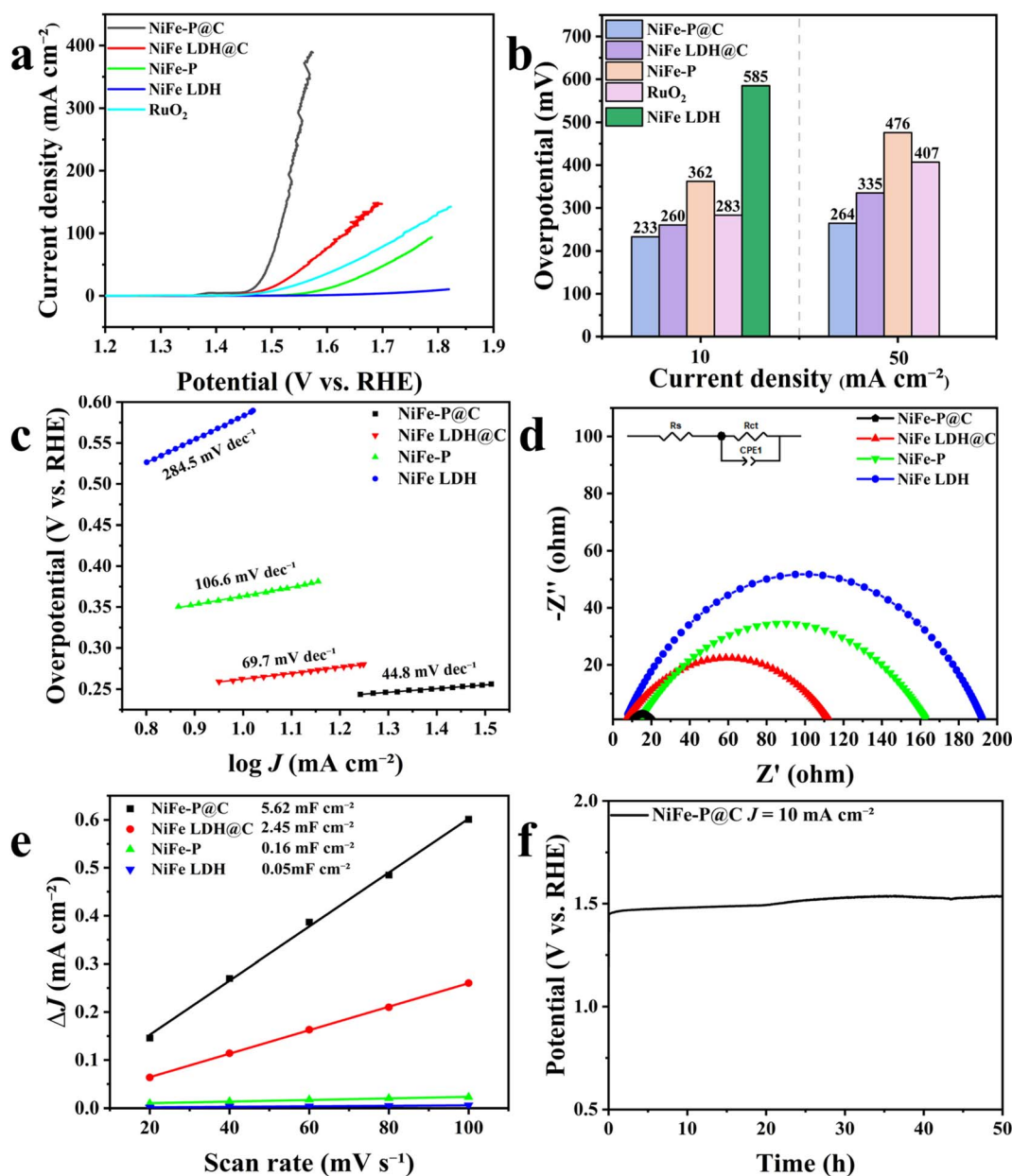


Fig. 4 (a) LSV polarization curves of NiFe LDH, NiFe-P, NiFe LDH@C, NiFe-P@C, and commercial RuO<sub>2</sub> in 1.0 M KOH. (b) OER  $\eta$  at 10 and 50 mA cm<sup>-2</sup>. (c) Tafel slopes. (d) Nyquist plots with the corresponding equivalent circuit model. (e)  $C_{dl}$  values of ECSAs. (f) Chronopotentiometry curve of NiFe-P@C.



862.7 and 880.8 eV.<sup>50</sup> Notably, shifts to higher binding energies in the Ni 2p spectrum after phosphidation reflect modifications in the Ni electronic configuration. In the Fe 2p spectra, peaks at 710.0 and 723.8 eV correspond to Fe<sup>2+</sup> 2p<sub>3/2</sub> and 2p<sub>1/2</sub>, while those at 712.6 and 725.8 eV are linked to Fe<sup>3+</sup> species (Fig. 3d).<sup>51</sup> A signal at 707.0 eV indicates Fe–P bonds,<sup>52</sup> confirming Fe<sub>2</sub>P formation. Compared with NiFe LDH@C, the appearance of Ni–P and Fe–P signals verifies successful phosphidation. As previously reported, Fe doping often boosts the OER activity of Ni-based catalysts.<sup>53</sup> Moreover, metal phosphides could undergo surface transformation under alkaline OER conditions, generating additional catalytically active sites.<sup>54,55</sup> Collectively, the XPS results reveal that NiFe–P@C comprises Ni(Fe)–P bonds from metal phosphides and P–O bonds corresponding to surface phosphate species. These phosphate entities, known for their flexible coordination properties, enhance the stability of transition metal sites under oxidative stress.<sup>42</sup> The coexistence of crystalline phosphide domains and amorphous phosphate layers forms a protective interface that enhances the catalyst's long-term structural integrity and electrochemical durability during OER operation. To gain insight into the local electronic interactions between NiFe–P and carbon support, high-resolution XPS of pure NiFe–P was analyzed. As presented in Fig. S3, Ni, Fe, P, and O were detected as the primary constituents. Compared with NiFe–P, the Ni and P peaks in NiFe–P@C shift slightly toward higher binding energies, whereas the Fe peak shifts marginally to lower binding energies. These variations indicate electron transfer from the carbon support to the phosphide species. This electronic coupling optimizes the local electronic configuration of NiFe–P, thereby enhancing its catalytic behavior. Furthermore, it strengthens phosphide anchoring on carbon, suppressing particle agglomeration or detachment during oxygen evolution and thereby enhancing long-term stability.

### 3.2. Electrocatalytic performances

The OER performance of the synthesized catalysts was assessed in 1.0 M KOH using a conventional three-electrode setup. The thermodynamic potential for OER is 1.23 V *versus* RHE, and  $\eta$  was calculated as  $\eta = E_{\text{RHE}} - 1.23$  V. To benchmark the electrocatalytic efficiency, LSV measurements were conducted for NiFe–P@C, bare NiFe LDH, NiFe LDH@C, and NiFe–P. As illustrated in Fig. 4a, unmodified NiFe LDH displays poor OER activity, requiring an  $\eta$  of 585 mV to reach 10 mA cm<sup>-2</sup>, mainly owing to aggregation and low conductivity. Incorporating carbon (NiFe LDH@C) markedly reduces  $\eta$  to 260 mV, reflecting improved charge transfer. Following phosphidation, NiFe–P exhibits an  $\eta$  of 362 mV, benefiting from the catalytic nature of NiFe–P. Notably, the NiFe–P@C catalyst exhibits the lowest  $\eta$  of 233 mV (Fig. 4b), indicating its superior activity. For comparison, commercial RuO<sub>2</sub> was evaluated under identical conditions with the same catalyst loading. As shown in Fig. 4a and b, NiFe–P@C exhibits lower overpotentials of 233 mV and 264 mV at current densities of 10 and 50 mA cm<sup>-2</sup>, respectively, whereas RuO<sub>2</sub> requires higher overpotentials of 283 mV and 407 mV to reach the same current densities. This result highlights the

superior intrinsic OER activity of NiFe–P@C compared to the noble metal benchmark. Prior to the LSV analysis, CV was employed to verify the catalyst's electrochemical stability. Moreover, the Tafel slope for NiFe–P@C is 44.8 mV dec<sup>-1</sup>, substantially lower than that for bare NiFe LDH (284.5 mV dec<sup>-1</sup>), NiFe–P (106.6 mV dec<sup>-1</sup>), and NiFe LDH@C (69.7 mV dec<sup>-1</sup>) (Fig. 4c). This enhanced performance stems from the high conductivity of the carbon matrix and the preserved 2D interconnected morphology that facilitates charge transport and mass diffusion.

EIS was employed to investigate interfacial charge-transfer behavior between the catalysts and the electrolyte. As depicted in Fig. 4d, the resulting Nyquist plots display characteristic semicircles reflecting the  $R_{\text{ct}}$  of each catalyst. Lower  $R_{\text{ct}}$  values indicate more efficient electron transfer and faster reaction kinetics. The  $R_{\text{ct}}$  values were obtained by fitting the impedance spectra with an appropriate equivalent circuit model, and the fitted parameters are provided in Table S2. Among all tested samples, NiFe–P@C demonstrates the lowest  $R_{\text{ct}}$  (10.77  $\Omega$ ), outperforming NiFe LDH@C (107.7  $\Omega$ ), NiFe–P (149.6  $\Omega$ ), and NiFe LDH (187  $\Omega$ ), thereby accounting for its enhanced electrocatalytic activity.

The ECSAs were further quantified based on  $C_{\text{dl}}$ , obtained from CV measurements in the non-faradaic potential region at varying scan rates (Fig. S4).<sup>56</sup> The NiFe–P@C demonstrates the highest  $C_{\text{dl}}$  of 5.62 mF cm<sup>-2</sup>, markedly exceeding that of NiFe LDH (0.05 mF cm<sup>-2</sup>), NiFe–P (0.16 mF cm<sup>-2</sup>), and NiFe LDH@C (2.45 mF cm<sup>-2</sup>) (Fig. 4e). In general, larger ECSA values and stronger intrinsic activity are beneficial for catalytic performance. The increased surface area of NiFe–P@C is attributed to its multidimensional architecture, which promotes efficient nanosheet separation and enhances the exposure of active sites. To assess the long-term OER stability, a chronopotentiometric ( $V-t$ ) test was conducted in 1.0 M KOH at a constant current density of 10 mA cm<sup>-2</sup>. As shown in Fig. 4f, the NiFe–P@C electrode maintains continuous operation for 50 h under these conditions, exhibiting overall stable performance with only a slight decay observed during prolonged electrolysis, indicating good electrochemical durability. The slight performance degradation can be attributed to the *in situ* surface reconstruction of NiFe–P into (oxy)hydroxide species, as well as minor active site loss and increased interfacial resistance during long-term electrolysis.

The enhanced OER performance of the NiFe–P@C electrocatalyst can be attributed to the synergistic integration of conductive carbon and NiFe phosphides. While bare NiFe LDH exhibits negligible catalytic activity and NiFe–P suffers from agglomeration and poor conductivity, the incorporation of carbon effectively addresses these limitations. The carbon scaffold enhances electrical conductivity and charge-transfer efficiency, while strong interfacial interactions between the carbon matrix and NiFe phosphides inhibit particle agglomeration and structural degradation during electrochemical cycling. This structural stability ensures sustained exposure of active sites and provides efficient pathways for electrolyte diffusion, collectively contributing to markedly improved OER performance.



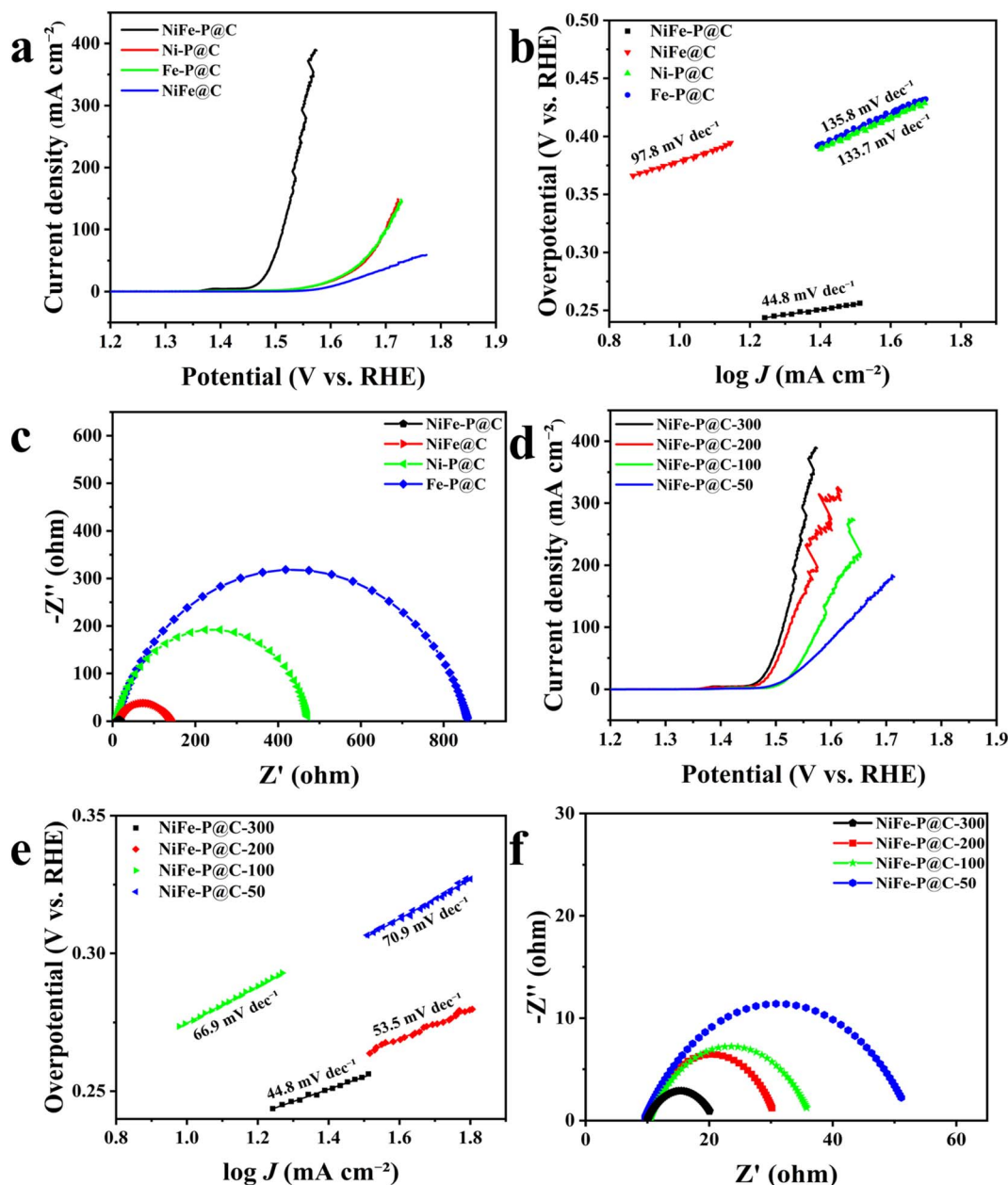


Fig. 5 (a) LSV polarization curves of NiFe-P@C, Ni-P@C, Fe-P@C, and NiFe@C in 1.0 M KOH, with corresponding (b) Tafel slopes and (c) Nyquist plots. (d) Electrocatalytic OER performance of NiFe-P@C-300, NiFe-P@C-200, NiFe-P@C-100, and NiFe-P@C-50 in 1.0 M KOH, with corresponding (e) Tafel slopes and (f) Nyquist plots.

The XRD patterns of Ni-P@C (Fig. S5a) and Fe-P@C (Fig. S5b) were further analyzed. During phosphidation of NiFe LDH, the resulting phases in NiFe-P@C are identified as Ni<sub>2</sub>P and Fe<sub>2</sub>P. However, individual phosphidation of Ni and Fe precursors yields Ni<sub>5</sub>P<sub>4</sub> (JCPDS No. 18-0883)<sup>57</sup> in Ni-P@C and FeP (JCPDS No. 65-2595)<sup>58</sup> in Fe-P@C, respectively. This difference arises from the distinct structural and chemical environments of the precursors. In the NiFe LDH framework, Ni and Fe cations are homogeneously distributed in the layered lattice, where strong electrostatic and coordination interactions restrict ion diffusion and alter the phosphidation pathways. This confinement favors the formation of kinetically stabilized

intermediate phases (Ni<sub>2</sub>P and Fe<sub>2</sub>P) rather than the thermodynamically favored Ni<sub>5</sub>P<sub>4</sub> and FeP formed in single-metal systems. In contrast, isolated Ni and Fe precursors undergo phosphidation without such spatial or chemical constraints, enabling transformation into the most stable phases under identical conditions. Therefore, the structural characteristics of the NiFe LDH precursor impose kinetic control over phase evolution, ultimately yielding distinct phosphide products compared with those derived from monometallic counterparts. As illustrated in Fig. 5a, NiFe-P@C achieves a current density of 10 mA cm<sup>-2</sup> at  $\eta$  of only 233 mV, which is substantially lower than those of Ni-P@C (348 mV), Fe-P@C (344 mV), and



NiFe@C (378 mV). Consistent with these results, the Tafel slopes (Fig. 5b) and  $R_{ct}$  values (Fig. 5c) reveal a similar trend, supporting the enhanced reaction kinetics of NiFe-P@C. Notably, Ni-P@C and Fe-P@C show nearly identical  $\eta$ , indicating comparable intrinsic activities. The improved OER behavior of NiFe-P@C could be attributed to the synergistic electronic modulation induced by the co-introduction of Ni and Fe species, which effectively alters the adsorption energetics of key reaction intermediates. This electronic tuning, combined with its structural advantages, enhances overall catalytic activity through two primary factors: (i) increased exposure of active

sites owing to high-surface-area nanostructures and (ii) accelerated charge transport enabled by interconnected porous pathways that facilitate efficient electrolyte access.

In addition, the influence of carbon content on the OER catalytic behavior was systematically examined by varying the carbon dosage (50, 100, 200, and 300 mg), corresponding to pump rates of 2.25, 4.5, 9, and 13.5 mL min<sup>-1</sup> during synthesis. This investigation focused on how carbon incorporation affects the interface between NiFe LDH nanosheets and carbon particles. The XRD patterns of NiFe-P@C-X samples with different carbon levels are shown in Fig. S6. Without carbon, diffraction

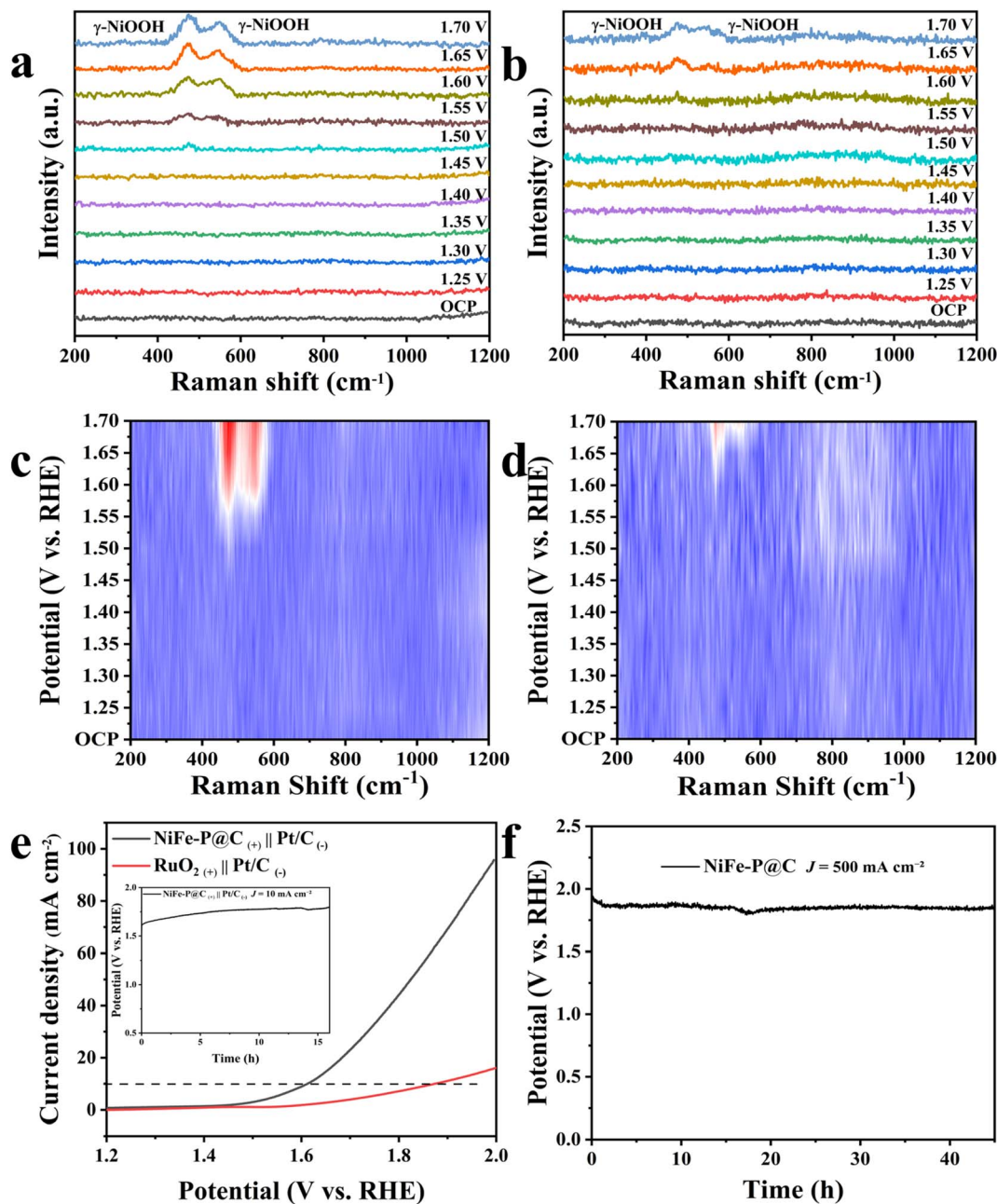


Fig. 6 *In situ* Raman spectra of (a) NiFe-P@C and (b) NiFe LDH@C during OER at applied potentials of 1.25–1.70 V versus RHE, with corresponding Raman contour plots shown in (c) and (d). (e) LSV curves of NiFe-P@C<sub>(+)</sub>||Pt/C<sub>(-)</sub> and RuO<sub>2</sub>(<sub>(+)</sub>)||Pt/C<sub>(-)</sub> for overall water splitting. The inset displays the corresponding chronopotentiometric response curves. (f) Chronopotentiometry curve of NiFe-P@C at 500 mA cm<sup>-2</sup>.



peaks corresponding to NiFe<sub>2</sub>O<sub>4</sub> (JCPDS No. 10-0325)<sup>59</sup> and NiO (JCPDS No. 47-1049)<sup>60</sup> are prominent, suggesting predominant oxide formation. Without carbon, NiFe LDH nanosheets aggregate, and limited contact with PH<sub>3</sub> gas (from NaH<sub>2</sub>PO<sub>2</sub>·H<sub>2</sub>O) during phosphidation results in insufficient phosphidation and enhanced oxide generation. Consequently, catalysts prepared without carbon primarily contain metal oxides formed during calcination. In contrast, increasing carbon content improves nanosheet dispersion and contact, allowing PH<sub>3</sub> to more effectively suppress oxidation and favor phosphide formation. The OER activity of NiFe-P@C-X samples synthesized with different carbon contents was subsequently investigated. Pristine NiFe-P exhibits  $\eta$  of 362 mV at 10 mA cm<sup>-2</sup> and a Tafel slope of 106.6 mV dec<sup>-1</sup>, indicating relatively poor performance, likely owing to low conductivity and limited catalytic site availability. In contrast, carbon-modified samples demonstrate substantially enhanced catalytic behavior (Fig. 5d and e). Compared with NiFe-P, incorporating carbon notably reduces the Tafel slope, highlighting the effectiveness of the face-to-face assembly strategy and indicating possible modification of the OER mechanism. With progressive increases in carbon content (50–300 mg), the electrocatalytic performance improves correspondingly (Fig. 5d). Notably, NiFe-P@C-300 displays superior activity, achieving  $\eta$  values of 241 mV at 10 mA cm<sup>-2</sup> and 264 mV at 50 mA cm<sup>-2</sup>. Moreover, this sample exhibits the lowest  $R_{ct}$  (10.77  $\Omega$ ; Fig. 5f), suggesting enhanced exposure of active sites and accelerated charge transport crucial for OER. These findings indicate that the structural reconstruction approach strengthens electronic interactions at the interface, thereby boosting catalytic efficiency. The improved durability is attributed to carbon, which reduces charge accumulation on the NiFe LDH surface during operation, effectively preventing structural degradation.

To elucidate the origin of the enhanced OER performance of NiFe-P@C, *in situ* Raman spectroscopy was employed to monitor surface intermediates under *operando* conditions. Spectra were collected for NiFe LDH@C and NiFe-P@C at applied potentials of 1.25–1.70 V *versus* RHE (Fig. 6a and b). At open-circuit potential and at potentials below 1.45 V *versus* RHE, no Raman-active surface species were detected for either catalyst. At 1.50 V *versus* RHE, two characteristic Raman bands emerged at approximately 477 and 556 cm<sup>-1</sup>, assigned to the E<sub>g</sub> bending mode ( $\delta$ [Ni–O]) and the A<sub>1g</sub> stretching mode ( $\nu$ [Ni–O]) of NiOOH, respectively.<sup>61</sup> With further increases in potential, the intensity and bandwidth of these peaks increased, reflecting the continuous generation and accumulation of NiOOH species during surface reconstruction. For NiFe LDH@C, a similar reconstruction behavior occurred (Fig. 6b), but the E<sub>g</sub> and A<sub>1g</sub> vibrations of NiOOH appeared only at 1.60 V *versus* RHE. This notable difference demonstrates that NiFe-P@C undergoes surface reconstruction to NiOOH at a lower potential, indicating faster reconstruction kinetics than NiFe LDH@C. Notably, no Raman signals corresponding to Ni(OH)<sub>2</sub> intermediates were detected across the potential range; instead, NiOOH formed directly once a critical potential was reached. The absence of Ni(OH)<sub>2</sub> and NiOOH signals at low potentials may result from the initial self-oxidation of NiFe-P@C, during which the Ni

oxidation state increases without forming Raman-active oxide phases. Subsequently, at approximately 1.50 V *versus* RHE, the oxidized Ni species (Ni<sup>3+</sup>) react directly with hydroxide ions in the alkaline electrolyte to generate NiOOH during OER.

As illustrated in the Raman contour plots (Fig. 6c and d), the NiOOH-related signals in NiFe-P@C exhibit a pronounced intensity enhancement at lower potentials compared with those in NiFe LDH@C, indicating a higher population of NiOOH active species. To quantitatively evaluate the extent of reconstruction, the relative intensities of the E<sub>g</sub> and A<sub>1g</sub> modes were used as descriptors for NiOOH formation. When normalized to the intensity at 1.70 V *versus* RHE, NiFe-P@C consistently showed higher relative intensities than NiFe LDH@C, confirming faster and more extensive surface reconstruction under identical electrochemical conditions. Overall, these *in situ* Raman results demonstrate that NiFe-P@C rapidly reconstructs into NiOOH during OER, generating a higher density of catalytically active NiOOH species at lower  $\eta$ . Such rapid and extensive reconstruction effectively prevents active site burial and directly contributes to the superior OER performance of NiFe-P@C. For comparison, the OER catalytic performance of the prepared sample is compared with that of other transition metal-based electrocatalyst materials from previous studies in Table S3. The results indicate that this study has advantages over similar work. To further evaluate the practical applicability, overall water-splitting performance was tested in a two-electrode system using the NiFe-P@C as the anode and Pt/C as the cathode. For comparison, a benchmark system consisting of RuO<sub>2</sub>||Pt/C was constructed under identical catalyst loading and preparation conditions. As shown in Fig. 6e, the NiFe-P@C-based electrolyzer requires a low cell voltage of 1.612 V to achieve 10 mA cm<sup>-2</sup>, which is significantly smaller than that of the RuO<sub>2</sub>||Pt/C system (1.874 V, without *iR* correction), demonstrating its superior performance. The water electrolysis durability of the NiFe-P@C||Pt/C electrolyzer was assessed by *V*-*t* curve at *J* = 10 mA cm<sup>-2</sup>. As shown in Fig. 6e, *V* increases to 1.77 V after 16 h, manifesting the acceptable stabilities of both electrodes. Based on these results, the NiFe-P@C materials described herein are a competent, nonprecious catalyst for full water electrolysis. As illustrated in Fig. 6f, the NiFe-P@C exhibits robust electrochemical durability, maintaining a high current density of 500 mA cm<sup>-2</sup> for over 45 h. A negligible fluctuation in potential (totaling approximately 5%) is observed during the long-term stability test. This minor variation could be attributed to the local temperature elevation at the electrode surface and the dynamic concentration gradients of the KOH electrolyte under industrial-level current densities.”

Electrochemical measurements experimentally confirm the enhanced OER activity of NiFe-P@C. To further understand the origin of this enhanced activity from an electronic-structure perspective, DFT calculations were performed, evaluating the Gibbs free energy evolution along the OER pathway. Based on optimized atomic models of NiFe LDH@C and NiFe-P@C (Fig. S7), differential charge density distributions were analyzed. As shown in Fig. 7a and b, pronounced charge redistribution occurs upon P incorporation, indicating strong



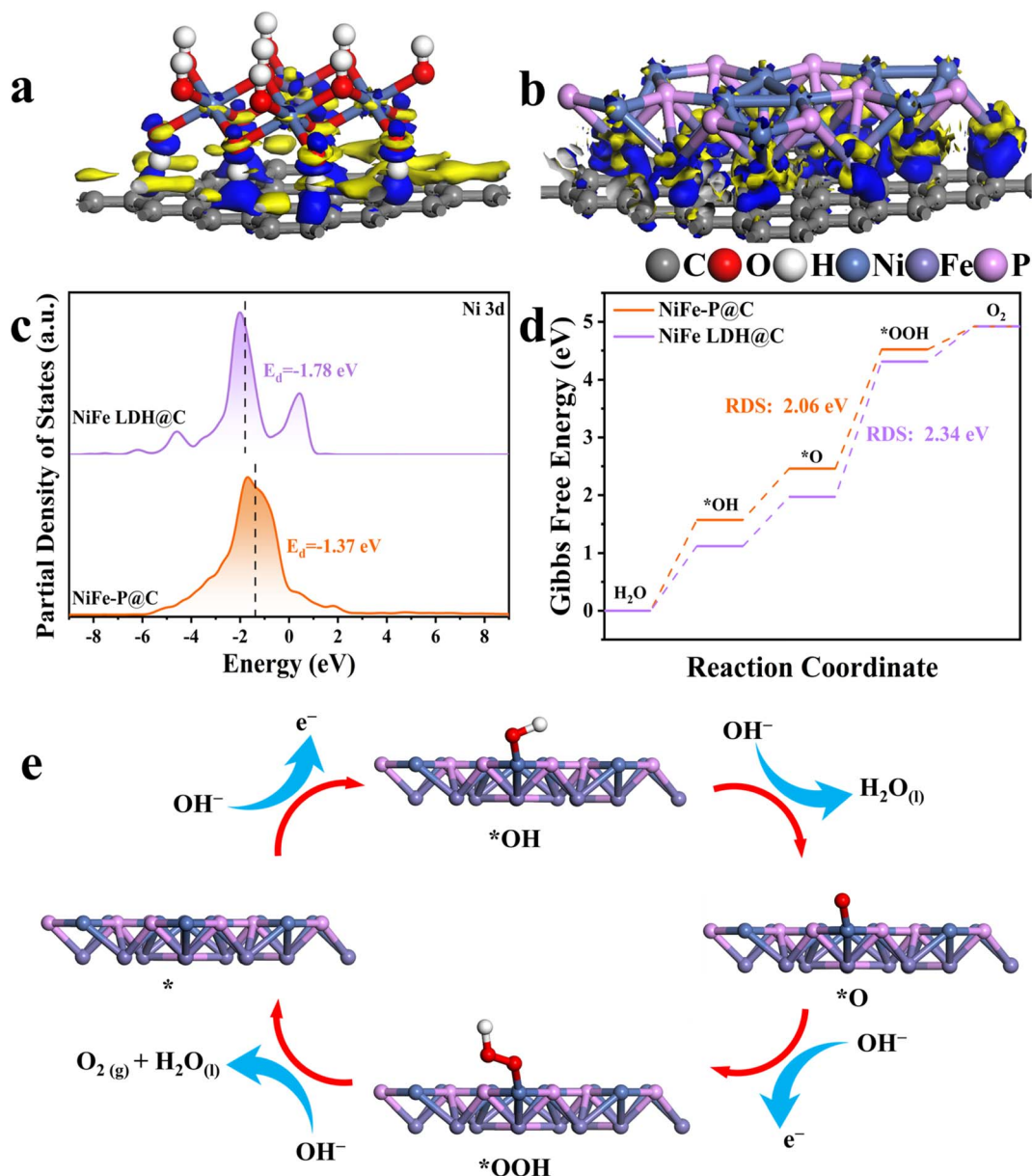


Fig. 7 Differential charge density distribution maps of (a) NiFe LDH@C and (b) NiFe-P@C. (c) Partial density of states of NiFe LDH@C and NiFe-P@C. (d) Gibbs free energy for the OER pathways on NiFe LDH@C and NiFe-P@C at  $U = 0$  V. (e) Adsorption configuration of key OER intermediates on NiFe-P@C.

electronic interactions between the doped P atoms and the NiFe LDH framework. This charge modulation is expected to influence the adsorption behavior of OER intermediates. According to the d-band center theory, the electronic states near the Fermi level ( $E_F$ ) govern the adsorption strength of reaction intermediates on catalyst surfaces. As illustrated in Fig. 7c, the d-band center of Ni 3d orbitals in NiFe-P@C ( $-1.37$  eV) is markedly upshifted toward  $E_F$  compared with that in NiFe LDH@C ( $-1.78$  eV), suggesting more optimal adsorption of oxygenated intermediates during OER. The electronic modulation induced by P doping also improves charge transport, thereby facilitating more efficient electron transfer between active sites and surface-adsorbed intermediates, collectively enhancing OER kinetics of

NiFe-P@C. Fig. 7d presents the calculated Gibbs free energy profiles for key OER intermediates (\*OH, \*O, and \*OOH) on both catalysts. For NiFe LDH@C and NiFe-P@C, the transformation from \*O to \*OOH is identified as the rate-determining step, characterized by the largest Gibbs free energy change ( $\Delta G$ ). Notably, NiFe-P@C exhibits a substantially reduced  $\Delta G$  value of 2.06 eV, compared with 2.34 eV for NiFe LDH@C, indicating a lower theoretical  $\eta$  requirement and thus superior intrinsic OER activity.

Based on these results, a plausible OER mechanism on NiFe-P@C is proposed (Fig. 7e). The reaction follows the conventional four-step proton-coupled electron transfer pathway involving the sequential formation of \*OH, \*O, and \*OOH



intermediates, ultimately yielding O<sub>2</sub>. Overall, the DFT calculations demonstrate that the enhanced OER performance of NiFe-P@C originates from P-induced electronic structure modulation, strengthened electronic coupling between P and Ni/Fe sites, and a markedly reduced energy barrier for the rate-determining step. In addition to the conventional adsorbate evolution mechanism (AEM), the oxide-pathway mechanism (OPM) has recently been proposed as an alternative OER pathway, where O<sub>2</sub> is generated *via* direct coupling of surface oxygen species (\*O), bypassing the formation of \*OOH intermediates.<sup>62</sup> Recent studies have suggested that OPM can be identified by the presence of a characteristic Raman signal at around ~1140 cm<sup>-1</sup>, which is assigned to the interfacial \*O–O\* species as a key reaction intermediate.<sup>63</sup> However, as shown in the *in situ* electrochemical Raman spectra of NiFe-P@C in this work (Fig. 6a–d), no discernible peak is observed in this region under OER conditions, indicating the absence of detectable \*O–O\* coupling intermediates. Combined with the lack of *operando* evidence and the stable electrochemical performance, the OER process over NiFe-P@C is therefore more reasonably attributed to the AEM pathway.<sup>40</sup> Nevertheless, the possible contribution of OPM cannot be completely excluded and requires further investigation.

The continuous coprecipitation of NiFe LDH on carbon substrates using a CT reactor demonstrates a fluid dynamics-driven strategy for electrocatalyst optimization. Rapid TVF ensures uniform LDH growth on carbon surfaces. This strategy effectively optimizes interfacial charge transport and reaction kinetics, resulting in improved catalytic activity and electrochemical stability of the composite electrocatalyst. The enhanced performance arises from the synergistic effects of shear-induced particle dispersion, which minimizes agglomeration, and strengthened substrate–catalyst adhesion. Overall, the method offers a scalable pathway for designing high-performance electrocatalysts with tailored interfacial architectures.

Despite the advantages of the proposed synthesis strategy, several potential limitations should be noted. The preparation of NiFe-P@C involves a two-step process consisting of the continuous coprecipitation of NiFe-LDH nanosheets on carbon supports in a Couette–Taylor flow reactor, followed by a phosphidation treatment at elevated temperature. Although the Taylor vortex flow reactor enables efficient mixing and uniform deposition of LDH nanosheets on the carbon surface, the use of such a reactor requires specialized equipment and precise control of hydrodynamic conditions, which may limit its accessibility compared with conventional batch synthesis methods. In addition, the phosphidation process requires high-temperature treatment and careful control of reaction parameters, which could affect the scalability and energy efficiency of the synthesis. Therefore, future studies may focus on simplifying the synthesis procedure and developing scalable continuous processes for the practical production of NiFe-based phosphide catalysts.

Looking forward, several directions can be pursued to further advance this catalyst system toward practical applications. Despite the promising activity demonstrated at both low

and high current densities (up to 500 mA cm<sup>-2</sup>) and in overall water splitting, rational electrode engineering will be essential to optimize mass transport and gas evolution dynamics under industrial operating conditions. Meanwhile, extended durability evaluation at high current densities is required to assess long-term operational stability. Beyond performance optimization, the flow-assisted Couette–Taylor synthesis strategy offers opportunities for the controlled construction of more complex multimetallic phosphides or heterostructured catalysts with tunable electronic properties. In addition, integrating *operando* spectroscopic techniques with theoretical simulations will be crucial to uncover dynamic structure–activity relationships under working conditions. Ultimately, the incorporation of such catalysts into practical electrolyzer devices and the evaluation of full-cell efficiency will be key steps toward scalable hydrogen production.

## 4. Conclusion

A novel NiFe-P@C electrocatalyst was successfully designed and synthesized *via* a two-step process: coprecipitation growth of NiFe LDH nanosheets on a carbon substrate using a continuous CT reactor, followed by phosphidation. This approach effectively combines the intrinsic catalytic activity of metal phosphides with the excellent conductivity and structural stability of carbon. The resulting NiFe-P@C catalyst demonstrates superior OER performance, with a low  $\eta$  of 233 mV and a Tafel slope of 44.8 mV dec<sup>-1</sup> at 10 mA cm<sup>-2</sup> in alkaline media. Its enhanced activity and durability are primarily attributed to NiFe growth on carbon, which facilitates rapid charge transfer and prevents nanosheet agglomeration, and the interconnected composite network, which ensures abundant active site exposure and efficient mass transport. This study provides a facile, scalable synthesis strategy for preserving favorable catalyst morphology while optimizing interfacial properties, offering valuable insights for developing advanced transition metal-based electrocatalysts for water splitting.

## Author contributions

Conceptualization and resources, T. Y.; methodology, validation, and formal analysis, T. Z. and Z. L.; data curation, K. K.; investigation, T. Z. and Z. L.; writing—original draft, T. Z. and Z. L.; writing—review and editing, T. Y.; project administration and funding acquisition, T. Y. All authors have read and approved the final manuscript.

## Conflicts of interest

There are no conflicts to declare.

## Data availability

The data supporting this article have been included as part of the supplementary information (SI). Supplementary information: Geometric parameters of the Couette–Taylor reactor, Simulated results, Elemental mapping images, Full-scan XPS



spectrum, Cyclic voltammograms, XRD patterns, optimized atomic models. Fig. S1 to S7; Tables S1 to S3. See DOI: <https://doi.org/10.1039/d6ta01534d>.

## Acknowledgements

This research was funded by the Nano & Material Technology Development Program through the National Research Foundation of Korea (NRF) funded by the Ministry of Science and ICT (RS-2024-00450102).

## References

- H. Tayyab, S. Liu, H. Zhang, R. Shen, Y. Liu, J. Jiang and B. Li, *J. Mater. Chem. A*, 2026, DOI: [10.1039/D5TA07323E](https://doi.org/10.1039/D5TA07323E).
- P. Varma, S. Saha, N. K. Banoth, A. Naidu, S. J. Lee, M. A. Bokinala, D. A. Reddy and U. Pal, *J. Mater. Chem. A*, 2026, DOI: [10.1039/D5TA10388F](https://doi.org/10.1039/D5TA10388F).
- M. Pal, R. Biswas, V. Trivedi, A. Saini and A. Dutta, *J. Mater. Chem. A*, 2026, **14**, 6106–6144.
- B. Jin, H. Wang, Y. Ji and J. Cheng, *J. Mater. Chem. A*, 2026, DOI: [10.1039/D5TA08516K](https://doi.org/10.1039/D5TA08516K).
- Z. Liu, S. Lee, T. Zhou, J. Yang and T. Yu, *J. Colloid Interface Sci.*, 2025, **692**, 137542.
- Z. Liu, H. Ma, T. Zhou, J. Yang and T. Yu, *J. Alloys Compd.*, 2024, **1002**, 175294.
- C. Rong, X. Huang, H. Arandiyana, Z. Shao, Y. Wang and Y. Chen, *Adv. Mater.*, 2025, **37**, 2416362.
- Y. Xiao, J. Fu, Y. Pihosh, K. Karmakar, B. Zhang, K. Domen and Y. Li, *Chem. Soc. Rev.*, 2025, **54**, 1268–1317.
- F. Wang, L. Xiao, Y. Jiang, X. Liu, X. Zhao, Q. Kong, A. Abdulkayum and G. Hu, *Mater. Horiz.*, 2025, **12**, 1757–1795.
- G. Chakraborty and S. Maity, *Adv. Synth. Catal.*, 2025, **367**, e202401239.
- S. M. Parsa, Z. Chen, H. H. Ngo, W. Wei, X. Zhang, Y. Liu, B.-J. Ni and W. Guo, *Nano-Micro Lett.*, 2025, **17**, 303.
- Y. Wang, M. Qiao, Y. Li and S. Wang, *Small*, 2018, **14**, 1800136.
- T. Kokulnathan, B. Honnappa, T.-J. Wang, K. M. A. Kumar and K. Sekar, *J. Colloid Interface Sci.*, 2025, **678**, 1036–1048.
- Z. Chen, Q. Li, H. Xiang, Y. Wang, P. Yang, C. Dai, H. Zhang, W. Xiao, Z. Wu and L. Wang, *Inorg. Chem. Front.*, 2023, **10**, 1493–1500.
- M. Qu, Y. Jiang, M. Yang, S. Liu, Q. Guo, W. Shen, M. Li and R. He, *Appl. Catal., B*, 2020, **263**, 118324.
- D. Liu, G. Xu, H. Yang, H. Wang and B. Y. Xia, *Adv. Funct. Mater.*, 2023, **33**, 2208358.
- Y. Li, Z. Dong and L. Jiao, *Adv. Energy Mater.*, 2020, **10**, 1902104.
- A. Ray, S. Sultana, L. Paramanik and K. Parida, *J. Mater. Chem. A*, 2020, **8**, 19196–19245.
- N. Ma, Y. Zhang, Y. Wang, C. Huang, J. Zhao, B. Liang and J. Fan, *Appl. Surf. Sci.*, 2023, **628**, 157225.
- Z. Wu, L. Huang, H. Liu, M. Li and H. Wang, *Nano Res.*, 2021, **14**, 2264–2267.
- R. Zhang, P. E. Pearce, Y. Duan, N. Dubouis, T. Marchandier and A. Grimaud, *Chem. Mater.*, 2019, **31**, 8248–8259.
- R. Li, J. Xu, C. Lu, Z. Huang, Q. Wu, J. Ba, T. Tang, D. Meng and W. Luo, *Electrochim. Acta*, 2020, **357**, 136873.
- L. Jia, G. Du, D. Han, Y. Wang, Y. Wang, H. Li, W. Zhao, S. Chen, M. Zhang and Q. Su, *ChemSusChem*, 2024, **17**, e202400997.
- J. Zhang, M. Sun, H. Guo, Z. Wang, J. Cheng, C. Lyu and Y. Liu, *J. Mater. Chem. A*, 2025, **13**, 29736–29775.
- Z. Liu, T. Zhou, J. Kim and T. Yu, *Dalton Trans.*, 2025, **54**, 11362–11370.
- H. Zheng, Q.-N. Wang, Z. Wang, W. Ma, G. Long, B. Chang, S. Liao and C. Li, *ACS Energy Lett.*, 2025, **10**, 678–684.
- S. Ge, P. Cheng, Y. Zhao, H. Jin, Y. Su, N. Li, J. Li, Z. Xiong, C. Feng and D. Shi, *Small*, 2025, **21**, 2406578.
- Q. Ni, S. Zhang, K. Wang, H. Guo, J. Zhang, M. Wu and L. Wang, *J. Mater. Chem. A*, 2024, **12**, 31253–31261.
- C. Liu, X. Cao, L. Chen, Q. Wang, B. Zhang, C. Liang, Y. M. Lam and L. Wang, *ACS Catal.*, 2025, **15**, 14983–14995.
- J. Wu, R. Chong, Z. Li, S. Xu, Y. Liu, X. He, J. Qian, J. Zhang, L. Wang and Z.-H. Zhang, *ACS Appl. Mater. Interfaces*, 2025, **17**, 52297–52306.
- T. Zhou, S. Lee, W.-S. Han, W.-S. Kim and T. Yu, *J. Environ. Chem. Eng.*, 2025, **13**, 115919.
- K. Gupta, J. H. Heo, S. H. Im and W.-S. Kim, *Chem. Eng. J.*, 2024, **481**, 148700.
- T. Zhou, H. Nam, J. Lee, W.-S. Han, W.-S. Kim and T. Yu, *ACS Appl. Mater. Interfaces*, 2025, **17**, 58288–58298.
- J.-Y. Jung, J.-G. Lee, Y.-K. Baek, Y.-D. Kim, J.-P. Hong and Y.-K. Kim, *J. Alloys Compd.*, 2019, **784**, 816–821.
- W. K. Park, H. Kim, T. Kim, Y. Kim, S. Yoo, S. Kim, D. H. Yoon and W. S. Yang, *Carbon*, 2015, **83**, 217–223.
- V. Kaushik, S. Wu, H. Jang, J. Kang, K. Kim and J. W. Suk, *Nanomaterials*, 2018, **8**, 587.
- J. P. Perdew, *Phys. Rev. Lett.*, 1997, **77**, 3868.
- D. Vanderbilt, *Phys. Rev. B*, 1990, **41**, 7892.
- D. Liu, Y. Yang, B. Xue, D. Zhang and F. Li, *ACS Appl. Mater. Interfaces*, 2024, **16**, 57017–57031.
- S. Tian, Z. Li, H. Wang, X. Du, G. Liu and J. Li, *Chem. Eng. J.*, 2025, **504**, 158701.
- M. Zhang, X. Chen and X. Yang, *J. Nanopart. Res.*, 2020, **22**, 96.
- L. Tan, J. Wang, S. Zhou, H. Zhu, J. Guo, Y. Chen, X. Li, Z. Dong, Q. Zhang and Y. Cong, *J. Colloid Interface Sci.*, 2025, **689**, 137263.
- M. Zhao, H. Li, W. Yuan and C. M. Li, *ACS Appl. Energy Mater.*, 2020, **3**, 3966–3977.
- Z. Z. Luo, Y. Zhang, C. Zhang, H. T. Tan, Z. Li, A. Abutaha, X. L. Wu, Q. Xiong, K. A. Khor and K. Hippalgaonkar, *Adv. Energy Mater.*, 2017, **7**, 1601285.
- G. Yilmaz, T. Yang, K. J. H. Lim, S. W. Chee, L. Shen, U. Mirsaidov, M. Bosman and G. W. Ho, *EcoMat*, 2023, **5**, e12312.
- Z. Q. Ge, J. Li, H. J. Zhang, C. Liu, G. Che and Z. Q. Liu, *Adv. Funct. Mater.*, 2024, **34**, 2411024.
- S. C. Huang, H. C. Yu, C. K. Peng, Y. G. Lin and C. Y. Lin, *Small*, 2025, **21**, 2408957.



- 48 R.-Q. Li, B.-L. Wang, T. Gao, R. Zhang, C. Xu, X. Jiang, J. Zeng, Y. Bando, P. Hu and Y. Li, *Nano Energy*, 2019, **58**, 870–876.
- 49 R. Luo, Y. Li, L. Xing, N. Wang, R. Zhong, Z. Qian, C. Du, G. Yin, Y. Wang and L. Du, *Appl. Catal., B*, 2022, **311**, 121357.
- 50 H. Liu, Z. Liu and L. Feng, *Nanoscale*, 2019, **11**, 16017–16025.
- 51 A. Fathollahi, T. Shahrabi and G. B. Darband, *J. Mater. Chem. A*, 2024, **12**, 9038–9054.
- 52 M. Jiang, H. Zhai, L. Chen, L. Mei, P. Tan, K. Yang and J. Pan, *Adv. Funct. Mater.*, 2023, **33**, 2302621.
- 53 C. Feng, M. B. Faheem, J. Fu, Y. Xiao, C. Li and Y. Li, *ACS Catal.*, 2020, **10**, 4019–4047.
- 54 A. Parra-Puerto, K. L. Ng, K. Fahy, A. E. Goode, M. P. Ryan and A. Kucernak, *ACS Catal.*, 2019, **9**, 11515–11529.
- 55 L. Su, X. Cui, T. He, L. Zeng, H. Tian, Y. Song, K. Qi and B. Y. Xia, *Chem. Sci.*, 2019, **10**, 2019–2024.
- 56 C. Wei, S. Sun, D. Mandler, X. Wang, S. Z. Qiao and Z. J. Xu, *Chem. Soc. Rev.*, 2019, **48**, 2518–2534.
- 57 P. Sivakumar, M. G. Jung, C. J. Raj, H. H. Rana and H. S. Park, *Int. J. Energy Res.*, 2021, **45**, 17005–17014.
- 58 S. Sultana, S. Mansingh and K. Parida, *J. Mater. Chem. A*, 2019, **7**, 9145–9153.
- 59 P. Sivakumar, R. Ramesh, A. Ramanand, S. Ponnusamy and C. Muthamizhchelvan, *J. Alloys Compd.*, 2013, **563**, 6–11.
- 60 Y. Zeng, Y. Meng, Z. Lai, X. Zhang, M. Yu, P. Fang, M. Wu, Y. Tong and X. Lu, *Adv. Mater.*, 2017, **29**, 1702698.
- 61 F. Shi, L. Xiao, Z. Zhou, X. Zhao, Y. Liu, J. Mao, J. Qin, Y. Deng and J. Yang, *Adv. Funct. Mater.*, 2025, **35**, 2501070.
- 62 Z.-H. Yin, H. Liu, J.-S. Hu and J.-J. Wang, *Natl. Sci. Rev.*, 2024, **11**, nwae362.
- 63 Z. Li, D. Wang, H. Kang, Z. Shi, X. Hu, H. Sun and J. Xu, *J. Mater. Chem. A*, 2025, **13**, 587–594.

